JOURNAL OF AIRCRAFT
Vol. 46, No. 5, September–October 2009

Evaluation of Computations and Transition Prediction Method for Aircraft High-Lift Configuration

Mitsuhiro Murayama,* Yuzuru Yokokawa,† and Kazuomi Yamamoto‡
Japan Aerospace Exploration Agency, Tokyo 182-8522, Japan
and
Yoshine Ueda§
Tokyo Business Service Company, Ltd., Tokyo 160-0023, Japan

DOI: 10.2514/1.34948

In this study, the three-dimensional flow computations over a realistic aircraft high-lift configuration with a flow-through nacelle with a pylon mounted beneath the main wing are performed using an unstructured mesh method to investigate the influence of the boundary-layer transition on the aerodynamic forces, the capability of a transition prediction method, and the influence of brackets to support the high-lift devices. First, the influence of the boundary-layer transition on the aerodynamic forces is shown by comparison of the computational results with/without the boundary-layer transition. Then a transition prediction method based on the e^N method and semi-empirical approaches is evaluated. The capability and areas to be improved are discussed. The influence of brackets to support the high-lift devices on the aerodynamic forces is also discussed. Interference of disturbed wakes by the slat supports to the flows on the main wing and flap is shown.

Nomenclature

C_D = drag coefficient
C_L = lift coefficient
$C_{L\,\max}$ = maximum lift coefficient
C_M = pitching moment coefficient
C_p = surface pressure coefficient
c = mean aerodynamic chord
L/D = lift-to-drag ratio
M_∞ = freestream Mach number
Re = Reynolds number
r = radius of curvature at the stagnation point
α = angle of attack
$\alpha_{\text{corrected}}$ = angle of attack after wind-tunnel wall corrections
Λ = leading-edge sweep angle

I. Introduction

EFFICIENT high-lift devices of an aircraft for takeoff and landing can produce large benefits on payload and fuel consumption [1,2]. Recent computational fluid dynamics (CFD) technologies for three-dimensional configurations are expected to improve the performance. However, a multi-element high-lift wing system that uses leading-edge slats and trailing-edge flaps complicates the flow features, due to boundary-layer transition from laminar to turbulent states, flow separation, interactions of the wake of each element, and so on. For a realistic high-lift configuration with an engine-nacelle pylon mounted under the wing, the stall phenomena are often largely affected by the complex flow interaction between the nacelle pylon and the high-lift devices. The flows derived from the spanwise gap between the inner slat end and fuselage also often affect the stall performance. The precise prediction of the aerodynamic forces such as $C_{L\,\max}$ and L/D for the three-dimensional high-lift configurations is still a challenging task. The physical understanding of the dominant aerodynamic phenomena and efforts to improve CFD for such complicated flows over realistic high-lift configurations are required in conjunction with experiments [3–12] to improve the performance.

In recent years, efforts to validate and improve CFD for high-lift systems have been promoted [4–15]. In the European EUROLIFT [6–12] project, developments of aerodynamic analysis for high-lift configurations have been intensively conducted in conjunction with experiments. The Civil Transport Team of Japan Aerospace Exploration Agency (JAXA), has conducted a research program to develop design technologies for advanced high-lift devices. In the research, the first wind-tunnel testing using an aircraft configuration, denoted as the JAXA Standard Model (JSM), deploying the high-lift devices with fuselage, long-cowl flow-through nacelle pylon, and flap track fairings was conducted from October 2005–February 2006 to increase the knowledge of high-lift flows over a realistic aircraft configuration, to improve the measurement technologies, and to provide the detailed and systematic experimental data, which can be disclosed for CFD validation [16–19]. The first CFD workshop using the data was also held in the domestic communities in October 2006. In March–April 2007, the second wind-tunnel testing was conducted to obtain additional data for laminar–turbulent transition of the boundary layer, nacelle interferences, additional aerodynamic devices, and so on. The third wind-tunnel testing was conducted in December 2007.

The aerodynamic forces for low-speed high-lift configurations at the flight high-Reynolds-number condition are often extrapolated from the results at the subscale wind-tunnel Reynolds number conditions. The maximum lift is expected to increase with increasing Reynolds number. However, the adverse Reynolds number effects often occur in some cases. The change of laminar–turbulent transition of boundary layer by Reynolds number can be one of the reasons to cause the adverse Reynolds number effects [20]. In the prediction of aerodynamic forces for high-lift configurations, the effect of the transition to the aerodynamic performance should be well estimated with the transition prediction methods. The flow interferences due to the nacelle pylon mounted beneath the main wing and high-lift devices can cause the undesirable effects. Therefore, the evaluation in the complete aircraft configuration is also important.

Presented as Paper 3924 at the 25th AIAA Applied Aerodynamics Conference, Miami, FL, 25–28 June 2007; received 3 October 2007; revision received 2 May 2008; accepted for publication 5 May 2008.

*Researcher, Civil Transport Team, Aviation Program Group, 7-44-1 Jindaiji-Higashi, Chofu. Senior Member AIAA.

†Researcher, Civil Transport Team, Aviation Program Group, 7-44-1 Jindaiji-Higashi, Chofu. Member AIAA.

‡Section Leader, Civil Transport Team, Aviation Program Group, 7-44-1 Jindaiji-Higashi, Chofu. Member AIAA.

§Engineer, 6-14-1, NishiShinjuku, Shinjuku.

There are several transition mechanisms for high-lift configurations. Transitions due to Tollmien–Schlichting (TS) instability, crossflow (CF) instability, and laminar separation bubbles should be considered. In addition, attachment-line contamination and relaminarization often occur due to large pressure gradients near the leading edges of slat, main wing, and flap. Bypass transition due to the wake flow from the fore wing element is also possible in the flows over multi-element high-lift configurations. These various transitions make it difficult to predict the onset of the transition. Several approaches to predict the transitions have been proposed and validated [9–12,21]. Numerical methods with higher fidelity, such as a method coupled with a three-dimensional boundary-layer code, have been also developed. For the computations over three-dimensional complete high-lift configurations, an unstructured mesh system is often used for the geometry complexity. Relatively simple approaches that do not require severe special mesh specifications such as highly dense mesh and grid orthogonality in the boundary layer are preferable for practical use in engineering. The applicability of the methods with several approximations to the complex high-lift flows should also have been validated.

For the validation study in the complete high-lift aircraft models, the additional brackets to support high-lift devices such as slat tracks and flap track fairings (FTFs) also complicate the flowfields. The disturbed or separated wakes due to the supports often affect the flows over the wing [22]. Such effects should be well estimated.

In this paper, the three-dimensional flow computations over a realistic aircraft high-lift configuration with a flow-through nacelle with a pylon mounted beneath the main wing, JSM, are performed using an unstructured mesh code. First, computational results with the fully turbulent flow and prescribed turbulent flow are compared to investigate the influences of laminar–turbulent transition of the boundary layer on the aerodynamic forces. Then a transition prediction method is evaluated by comparison of the transition lines with the experimental results. A prediction method based on the e^N method is used for transitions due to TS, CF, and laminar separation bubbles. For the stability analysis, laminar boundary layers are recalculated at several sections based on the computed surface pressures. For the prediction of attachment-line contamination and relaminarization, semi-empirical approaches are employed. Finally, the influence of brackets to support the high-lift devices is investigated by comparison between the computational results with/without the brackets.

II. Computational Method

A. Flow Solver

As the unstructured mesh generator and flow solver, TAS (Tohoku University Aerodynamic Simulation) code [23,24] is used in this study. TAS_Mesh is the mesh generator with graphical user interface tools [25–27]. It can generate nearly isotropic triangular surface mesh with a direct advancing-front method [25]; tetrahedral volume mesh using Delaunay tetrahedral meshing [26]; and hybrid volume mesh composed of tetrahedrons, prisms, and pyramids for viscous flows with high Reynolds numbers [27]. In TAS_Flow, Navier–Stokes equations are solved on the unstructured mesh by a cell-vertex finite volume method. The Harten–Lax–van Leer–Einfeldt–Wada method [28] is used for the numerical flux computations. The second-order spatial accuracy is realized by an unstructured MUSCL scheme [29]. The lower/upper symmetric Gauss–Seidel implicit method [30] is used for time integration.

In this study, the Spalart–Allmaras one-equation turbulence model [31] with several minor modifications is used to simulate turbulent flows. The model is used without the trip term for transition and $ft2$ function, which tends to suppress the production of eddy viscosity due to numerical error. The production of eddy viscosity starts with the freestream value. A modification that reduces the eddy viscosity in the regions of high vorticity [32] is also used. In the modification, a simple combination using the minimum of the vorticity $\Omega = \sqrt{2\Omega_{ij}\Omega_{ij}}$ and strain rate $\hat{S} = \sqrt{2s_{ij}s_{ij}}$ is used in the modification of the production term [32] as follows:

$$S = \Omega + \min(0, \hat{S} - \Omega) \tag{1}$$

The modified model computes turbulent vortical flow without adding much dissipation to the vortex core.

If some laminar regions are prescribed to simulate boundary-layer transition in computations, the term S in the production term is set to zero in the regions. In the specification, the generation of turbulent eddy viscosity is limited in the prescribed regions, whereas the advection from upstream is allowed.

The computations were carried out on a Fujitsu PRIMEPOWER HPC2500 multiprocessor, which is the main machine of Numerical Simulator III in JAXA [33].

B. Boundary-Layer Transition Prediction Method

For high-lift configurations, transitions due to TS instability, CF instability, and laminar separation bubbles should be considered. In addition, attachment-line contamination and relaminarization often occur due to large pressure gradients near the leading edges of the slat, main wing, and flap. Bypass transition due to the wake flow from the fore wing element can also be an important factor in the flows over multi-element high-lift configurations.

As a boundary-layer transition prediction code for transitions due to TS and CF instability and laminar separation bubbles, the LSTAB code [34–36] is used. LSTAB code has been developed and validated through the NEXST-1 (National Experimental Supersonic Transport) project at JAXA [37,38]. LSTAB code uses an e^N method based on a linear stability theory of laminar boundary layer.

In LSTAB code, a parallel flow approximation is applied to the laminar boundary layer, and the small disturbance of a following plane wave type is assumed:

$$q'(x, y, z, t) = \tilde{q}(y)\exp[i(\alpha x + \beta z - \omega t)], \qquad \alpha = \alpha_r + i\alpha_i$$
$$\beta = \beta_r + i\beta_i, \qquad \omega \equiv 2\pi f \tag{2}$$

where q' represents physical variables such as velocity, temperature, and density, etc.; x, y, and z represent a local streamline direction at the edge of the boundary layer, a boundary-layer thickness direction, and a crossflow direction perpendicular to them; α_r and β_r are the wave number vectors of disturbance in the x and z directions, respectively; α_i and β_i are amplification rates in the x and z directions, respectively; and f is the frequency of disturbance.

Next, linearization is carried out by considering small q'. If the boundary condition is imposed that the disturbance is 0 at the edge of the boundary layer and the wall, the simultaneous equation that forms an eigenvalue problem will be derived. Although this equation is solved under the specified Reynolds number and f at every x station, certain auxiliary equations are needed because the simultaneous equation includes four independent variables.

Furthermore, an e^N method is applied to predict the transition locations. The onset of transition location is specified as the location at which the amplitude of small disturbance, A, increases e^N times that at a neutral stability point A_0. In this assumption, the N factor is obtained by the following equation:

$$N \equiv \ln\left(\frac{A}{A_0}\right) = \int_C (-\alpha_i \mathrm{d}x - \beta_i \mathrm{d}z) \equiv \int_C \mathrm{d}o \tag{3}$$

where C represents an integral path. For the selection of the path in three-dimensional flow, the following assumption is adopted for the simplicity.

First, because a small disturbance is assumed, it is thought that the disturbance is basically carried along a local streamline. Therefore, we focus on the integral path limited in the local streamline direction ($dz = 0$) and then use the following equation:

$$d\sigma = -\alpha_i(\psi, \bar{\psi}\colon Re(x), f)dx, \qquad \psi \equiv \tan^{-1}\left(\frac{\beta_r}{\alpha_r}\right)$$
$$\bar{\psi} \equiv \tan^{-1}\left(\frac{\beta_i}{\alpha_i}\right) \tag{4}$$

where ψ means a propagation direction of a wave number, and $\psi = 0$ and 90 deg correspond to a local streamline direction and crossflow direction, respectively.

Next, the assumption of $\bar{\psi} = 0$ deg was used because the N factor might become large in most cases with $\bar{\psi} = 0$ deg, which is shown in the study of the influence on eigenvalue α_i [36]. Finally, to decide the relation between ψ and α_i, the following envelope method, which was widely used, was applied:

$$N(Re(x)\colon f) = \int_{C_{\mathrm{los}}} \max\nolimits_{\psi}[-\alpha_i(\psi\colon Re(x), f)]\mathrm{d}x \tag{5}$$

where C_{los} represents an integral path along the local outer streamline. Here, $N(x)$ curves are evaluated for every f using the equation. Further, the following equation, which represents the envelope of these N curves, is used as the final transition decision:

$$N_{\mathrm{envelope}} = \max\nolimits_f[N(Re(x)\colon f)] \tag{6}$$

The transition onset is predicted using a threshold of N factor based on a database. In the process, the distinction between the transition due to TS and CF instability is not a concern. The distinction is evaluated afterward based on the dominant wave angle if necessary.

The stability analysis is performed at several streamwise sections. For the stability analysis, velocity profiles in the boundary layer are required at each section. Extracting the accurate velocity profiles directly from CFD results requires a highly dense grid in the boundary layer. In the present study, the laminar boundary layer is recalculated based on the computed C_p using the Kaups and Cebeci method [39] in LSTAB code at each section. The method employs the conical flow approximation to simplify the three-dimensional boundary-layer equations. In the boundary-layer computations, laminar separation is detected based on the shape factor H. In the present method, it is assumed that the transition starts just before the detected location of the laminar separation if the transition due to TS and CF instability does not occur.

For the prediction of attachment-line contamination and relaminarization, semi-empirical approaches are employed. Attachment-line contamination is predicted using the attachment-line Reynolds number $\bar{R}^*$ based on Poll's criterion [40] in Eq. (7). In Eq. (7), subscript e means the values at the boundary-layer edge. However, it is difficult to obtain the precise definitions at the boundary-layer edge in the present Reynolds-averaged Navier–Stokes (RANS) mesh results. To simplify the estimation, an infinite swept cylindrical approximation of the flow is used near the attachment line. With the approximation, the precise definitions at the boundary-layer edges are not required as in Eqs. (8) and (9). The leading-edge sweep angle Λ and radius of the curvature at the stagnation point r are main factors in Eq. (7). Contamination will occur if the value of $\bar{R}^*$ exceeds 245 ± 20:

$$\bar{R}^* \equiv \frac{V_e \eta^*}{\nu^*} = \sqrt{\left[(V_e)^2_{s_w=0}\right] \Big/ \left[\nu^* \left(\frac{dQ_e}{ds_w}\right)_{s_w=0}\right]} \tag{7}$$

$$\left(\frac{dQ_e}{ds_w}\right)_{s_w=0} = \frac{2(U_\infty \cos\Lambda)}{r} \tag{8}$$

$$(V_e)_{s_w=0} = U_\infty \sin\Lambda \tag{9}$$

$$\bar{R}^* \geq 245 \pm 20\text{: contamination} \tag{10}$$

Relaminarization is predicted using parameter $\bar{K}$ [41], which indicates the acceleration strength of flows. Relaminarization will occur if the value of $\bar{K}$ exceeds 5×10^{-6}. For three-dimensional flow, the analysis using this prediction method should be conducted along the external streamlines. In the present study, the analyses for attachment-line contamination and relaminarization are performed at several sections normal to the leading edges:

$$\bar{K} = \frac{\nu *}{Q_e^2}\frac{dQ_e}{ds_w} \tag{11}$$

$$\begin{aligned} \bar{K} &> 10^{-6}\text{: start of relaminarization} \\ &> 5 \times 10^{-6}\text{: relaminarization} \end{aligned} \tag{12}$$

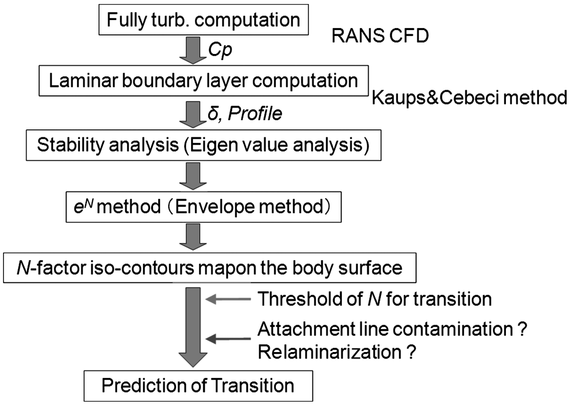

Fig. 1 Procedure of transition prediction method.

The analysis procedure for the present study is summarized in Fig. 1. In the present study, the first CFD computation to obtain C_p at each section is performed assuming fully turbulent flows. Next, the modules of the transition prediction, LSTAB, and the evaluation of the experimental criteria for attachment-line contamination and relaminarization are separated and the whole transition prediction process is not fully automated. Therefore, the process is done as the postprocessing after the CFD computation. Although this procedure should be repeated until the change of the transition locations is converged, the results after only one cycle are presented here.

For the wind-tunnel tests used in the present study, the threshold of the N factor is expected to be 4.0–6.0 based on the past experimental results. In this study, $N = 4.0$ is used for the threshold.

III. Model Geometry and Computational Conditions

Figure 2 shows the wind-tunnel model tested in October 2005–February 2006 at the JAXA 6.5 × 5.5 m low-speed wind tunnel (JAXA-LWT1) [16–19]. JAXA-LWT1 is an atmospheric closed-circuit wind tunnel with an octagonal cross section. The test was carried out to provide the experimental data for CFD validation and to investigate the flow physics for realistic aircraft configurations deploying the high-lift devices. The model was designed assuming a

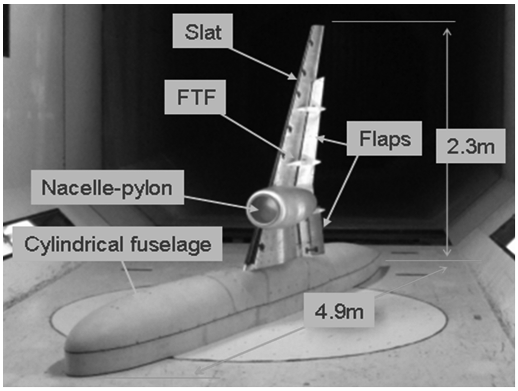

Fig. 2 Wind-tunnel testing model in JAXA-LWT1.

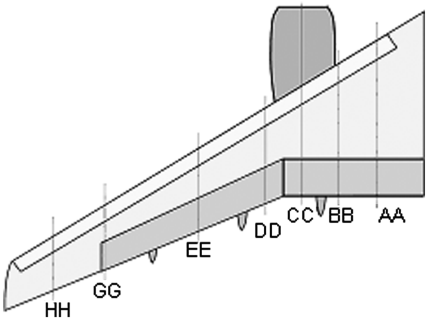

Fig. 3 Cross sections for static pressure measurement.

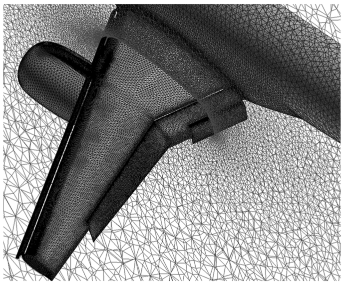

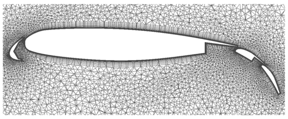

(i) An inboard span location

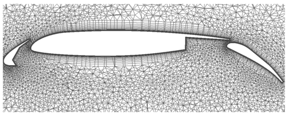

(ii) An outboard span location

a) Bird's-eye view **b) Cross-sectional view**

Fig. 4 Computational mesh without FTFs and brackets to support the high-lift devices.

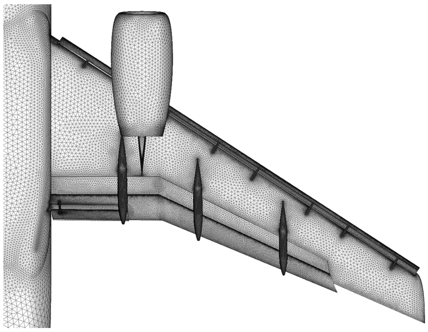

Fig. 5 Computational mesh with FTFs and brackets to support the high-lift devices.

100-passenger-class civil jet aircraft. The scale of the wind-tunnel model is roughly $1/6$ of the assumed aircraft. The lengths of the wing half-span and fuselage are 2.3 and 4.9 m, respectively. The mean aerodynamic chord length (MAC) of this model is 0.529 m. The aspect ratio of the wing is 9.42 and the leading-edge sweep angle is 33 deg. The model has a leading-edge slat supported by eight slat brackets, a double-slotted flap inboard and a single-slotted flap outboard with a circular fuselage, a flow-through nacelle with a pylon mounted beneath the main wing, and three FTFs, as shown in Fig. 2. For the landing setting, the deflection angles of the slat, flap, and aft flap are 25, 35, and 20 deg, respectively. In the testing, various kinds of measurements were conducted to verify CFD analysis in detail [16–19]. Five-component aerodynamic forces, surface pressure with pressure taps, and pressure-sensitive paint were obtained. Static surface pressures using 456 static pressure taps were measured at seven cross sections on the wing, four cross sections on the fuselage, and several points on the pylon. Figure 3 shows the locations of the cross sections for the static pressure measurement on the wing. Surface flow visualizations were carried out with tuft, oil flow, and china clay. In the testing, moreover, unsteady pressure, velocity distribution around the model using particle image velocimetry, and aeroacoustic noise sources using phased-array microphones were also measured.

Figures 4 and 5 show the computational unstructured meshes without/with FTFs and brackets to support slats and aft flap (configuration 1 is without FTFs and without slat support; configuration 2 is with FTFs and with slat support). The unstructured meshes have 5.8 and 7.4 million mesh points, respectively. Unstructured mesh with only brackets to support slats (configuration 3 is without FTFs with slat support) are also generated. The number of the mesh points is 7.2 million. The minimum grid spacing in the normal direction to the wing surface is $0.02/\sqrt{Re}$. Only one or two cells are placed on the blunt trailing edges. In the current computations, M_∞ is 0.175 and Reynolds number is 2.1×10^6 based on the MAC.

IV. Results

A. Comparison Between the Computations of Fully Turbulent Flows and Flows with Laminar Regions

First, the computational results assuming fully turbulent flows and flows with prescribed laminar regions are compared with the wind-tunnel testing data. The computational results without FTFs and brackets to support the slats and aft flap are compared. The prescribed laminar regions are based on the experimental observations by the

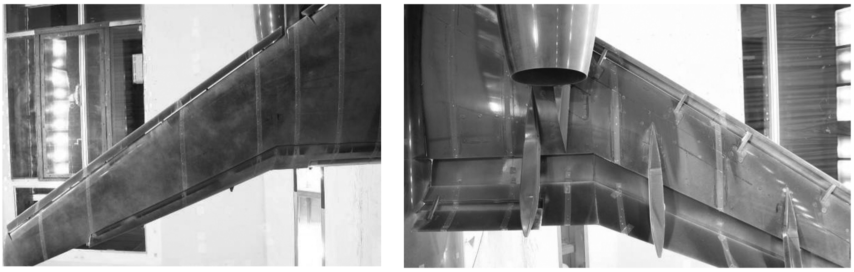

a) $\alpha_{corrected} = 4.43°$

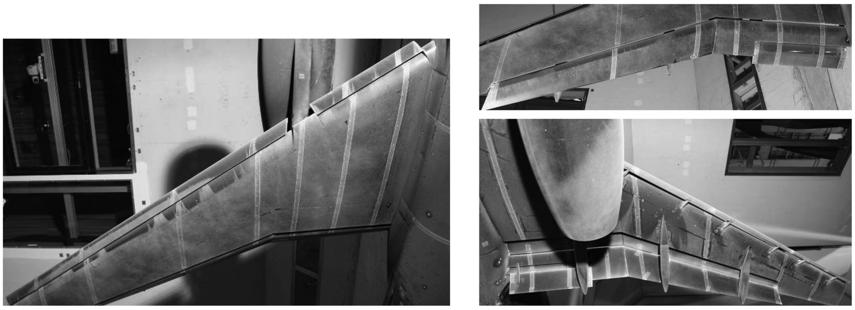

b) $\alpha_{corrected} = 10.55°$

Fig. 6 Visualization of boundary-layer transition by china clay.

(i) Upper surface **(ii) Lower surface** **(i) Upper surface** **(ii) Lower surface**

a) $\alpha = 4°$ **b) $\alpha = 10°$**

Fig. 7 Regions of boundary-layer transition assumed in computations (Blue: Laminar, Gray: Turbulent).

china-clay visualization. The china-clay visualization results at $\alpha_{\text{corrected}} = 4.43$ and 10.55 deg are shown in Fig. 6. The white regions are turbulent, and black regions are laminar. In the experiments, the boundary layer on the lower surface of the main wing became turbulent locally by the influence of the slat supports and FTFs. Figure 7 shows the prescribed laminar regions assumed in computations. In the computations, the laminar regions on the lower surface of the main wing are assumed, as shown in Fig. 7. In addition, the whole lower surface of the flap is assumed to be laminar in the computations.

Figure 8 shows C_L-α, C_L-C_D, and C_M-α for computed results and experimental data after the correction of the wind-tunnel wall and other interference. As for C_L-α, both computational results show good agreement with the experimental data at moderate angles of attack, although the lift slope before the stall has slight differences, whereas the stall angle of attack and $C_{L\,\max}$ are slightly overestimated in the computations. Decrease of C_L due to the stall in the computational result is also larger than that in the experimental results. The results with laminar regions show higher C_L, especially at higher angles of attack, and the slope of C_L-α shows better agreement with experimental results. However, the consideration of the boundary-layer transition does not improve the stall prediction in the present case.

As for C_M, the overall tendency of the computational results agrees well with the wind-tunnel results, including the change of the gradient after the stall, although a constant deviation of C_M is seen in the computations. As for C_L-C_D, both computational results overestimate C_D. Computational results with boundary-layer transition show a decrease of C_D by 40 drag counts (1 drag count equals 1×10^{-4}). The amount of the influence of the boundary-layer transition upon the drag prediction is shown in the computations. However, the difference with experimental results is still large. This result shows a possibility that the difference comes from insufficient grid resolution against the complicated model geometry in the computations.

Figures 9 and 10 show the comparisons of C_P at $\alpha = 4$ and 10 deg. At $\alpha = 4$ deg, computational results show good agreement with experimental results at all sections in Fig. 10. Designed wide and flat suction peaks near the leading edge of the main wing are well predicted. The results considering the specified transition flows show a little difference at the suction peaks. At $\alpha = 10$ deg, the difference between the fully turbulent and specified transition flows is larger. The results of the specified transition flow show larger suction peaks by the acceleration of flow near the main and flap leading edges and better agreement with experimental results. At both angles of attack, the difference at section H-H near the wing tip between experimental and computational results is slightly larger on the upper surface near the trailing edge of the main wing. This is due to the difference in the flow separation near the wing tip.

Figures 11 and 12 compare the surface flow patterns between the experimental and computational results with specified laminar

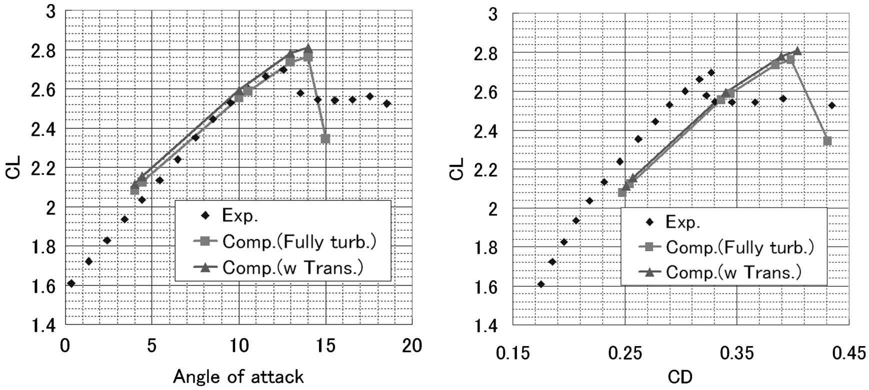

a) C_L-α **b) C_L- C_D**

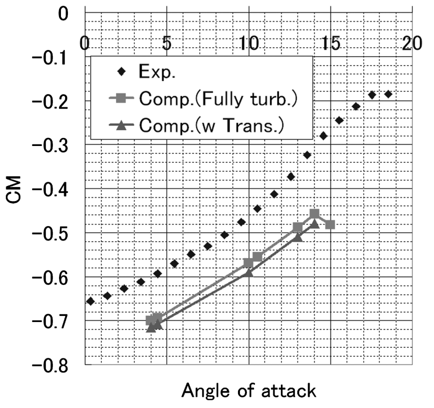

c) C_M-α

Fig. 8 Comparison of aerodynamic forces.

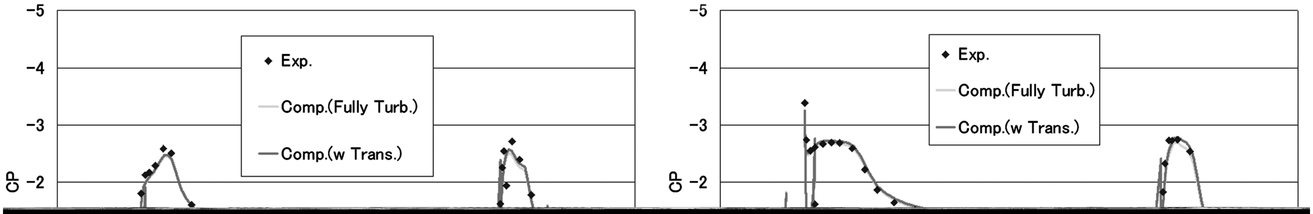

[redacted]

Fig. 9 Surface pressure distributions at $\alpha = 4\,\text{deg}$.

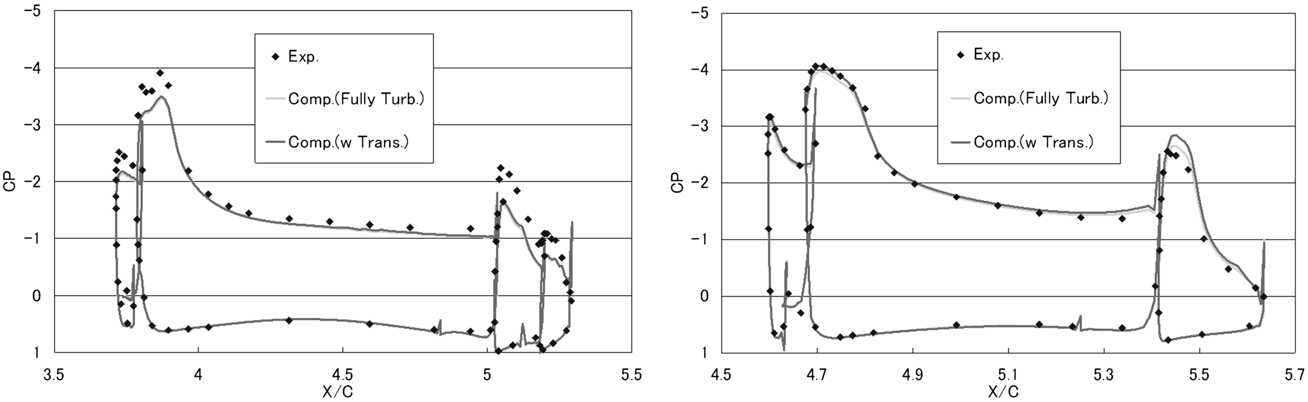

a) Section B-B

b) Section E-E

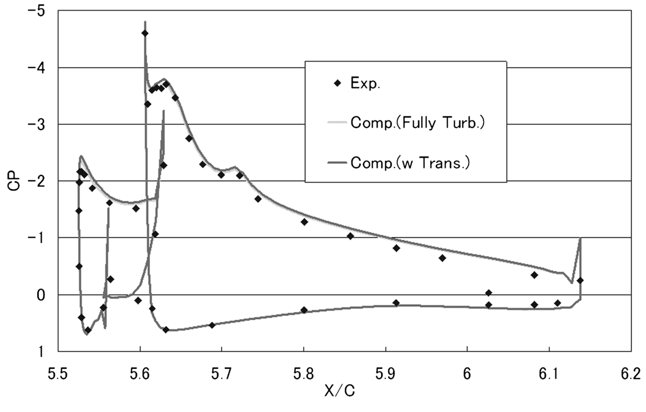

c) Section H-H

Fig. 10 Surface pressure distributions at $\alpha = 10\,\text{deg}$.

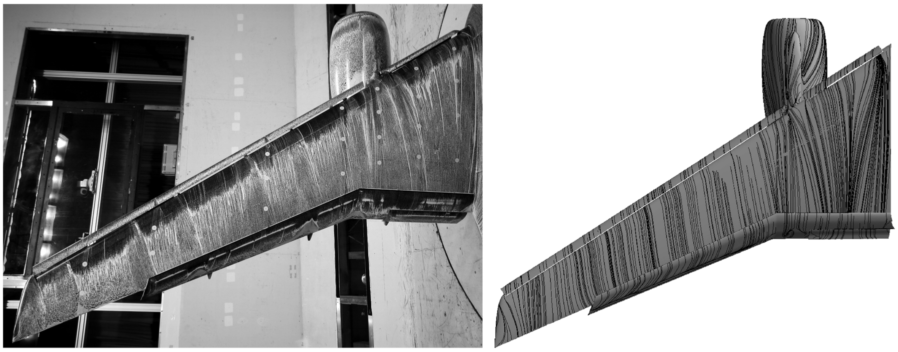

a) Experimental result b) Computational result

Fig. 11 Comparison of surface flow pattern at $\alpha = 4\,\mathrm{deg}$ (experimental data is at $\alpha_{\mathrm{corrected}} = 4.43\,\mathrm{deg}$).

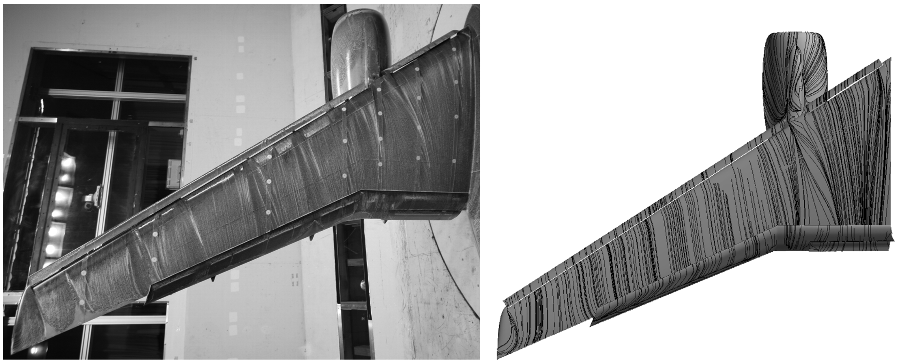

a) Experimental result b) Computational result

Fig. 12 Comparison of surface flow pattern at $\alpha = 10\,\mathrm{deg}$ (experimental data is at $\alpha_{\mathrm{corrected}} = 10.55\,\mathrm{deg}$).

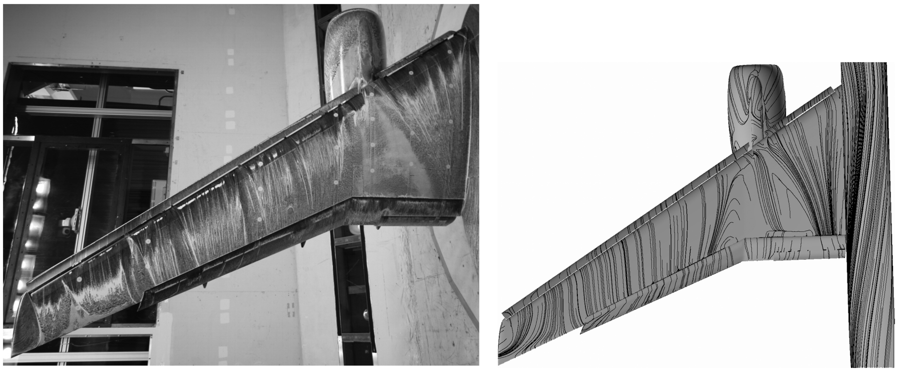

a) Experimental result b) Computational result

Fig. 13 Comparison of surface flow pattern at $\alpha = 15\,\mathrm{deg}$ (experimental data is at $\alpha_{\mathrm{corrected}} = 15.54\,\mathrm{deg}$).

regions at $\alpha = 4$ and 10 deg. The compared angles of attack are a little different between the experimental and computational results due to the wind-tunnel data correction. However, the small difference of α does not change the flow features visualized on the oil flows. At angle of attack $\alpha = 4$ deg, the computational result shows good agreement with the experimental results. The interference of the nacelle pylon is small at this low angle of attack. On the other hand, there are several local differences. The experimental result clearly shows the influence of the slat supports and FTFs on the upper side of the main wing and flaps. Near the trailing edge of the wing tip, only the experimental result shows a little flow separation of the main wing. It is considered that the separation causes the disagreement of surface pressure distribution at the H-H cross section in Figs. 9c and 10c. The difference of the surface flow on the flaps is relatively larger. The larger local flow separations by the influence of FTFs appear on the flap in the experimental results. At an angle of attack of 10 deg in Fig. 12, the difference between the experimental and computational results becomes larger near the wing tip. The difference of the flow separation seems to be produced by the presence of the slat supports.

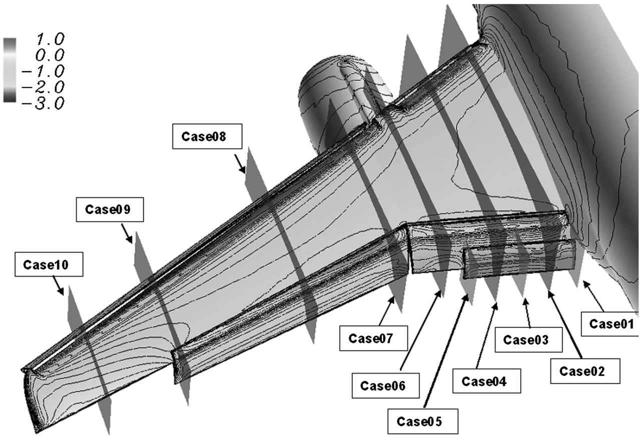

Fig. 14 Streamwise sections for transition prediction analysis for TS and CF instabilities and laminar separation bubbles using LSTAB code.

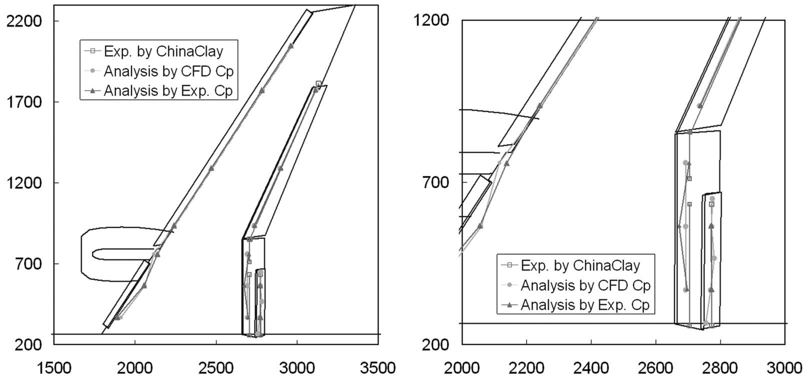

a) Overview b) Inner flap

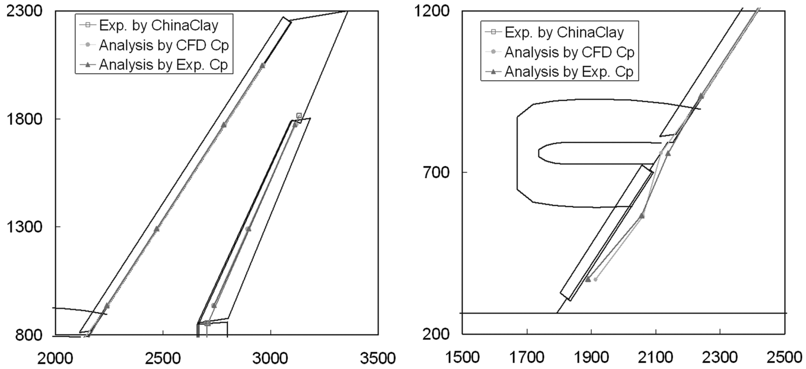

c) Outer wing and flap d) Inner wing

Fig. 15 Comparison of transition locations; Experimental result is at $\alpha_{\text{corrected}} = 4.43\,\text{deg}$ and predicted results are at $\alpha = 5\,\text{deg}$. (Transition lines for the slats are not plotted because flows on the upper side are almost laminar until the trailing edge both experimental and predicted results. Transition lines of experimental results for main wing are not plotted because the flow on the main wing is turbulent from the leading edge.)

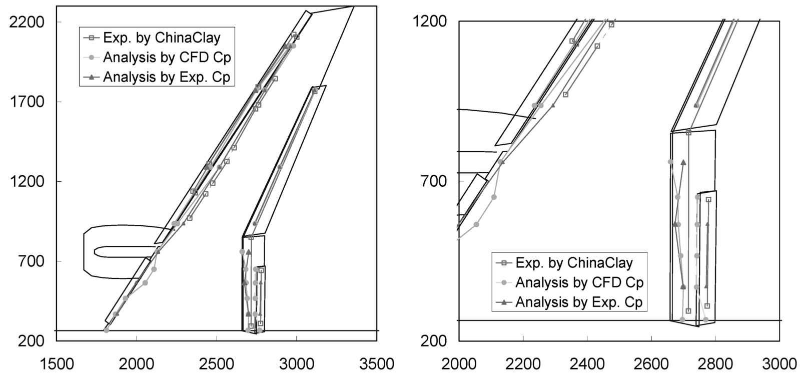

a) Overview b) Inner flap

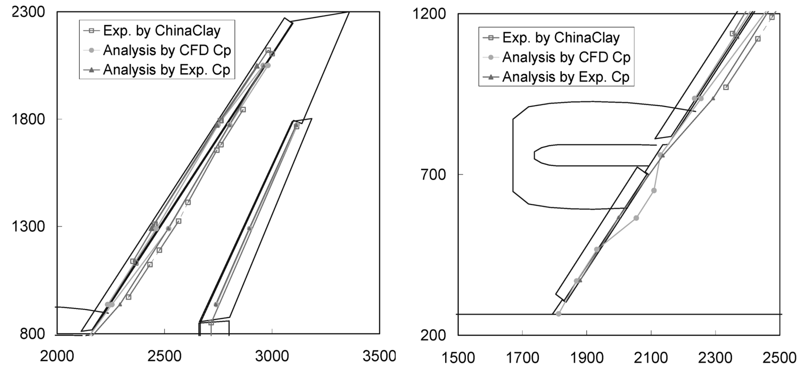

c) Outer wing and flap d) Inner wing

Fig. 16 Comparison of transition locations; Experimental result is at $\alpha_{\text{corrected}} = 10.55\,\text{deg}$ and predicted results are at $\alpha = 10\,\text{deg}$. (Transition lines for the inner slat are not plotted because flows on the upper side are almost laminar until the trailing edge both experimental and predicted results. Transition lines of experimental results for the inner main wing are not plotted because the flow on the inner main wing is turbulent from the leading edge.)

Figure 13 compares the surface flow patterns at an angle of attack of 15 deg. Large separation is visible on the main wing after the nacelle pylon in the experimental results. The computational result also predicts the same separation phenomena. The separation affects the whole stall performance. The separation pattern is well captured in the computation, whereas the separation size is predicted to be relatively larger in the computations. It results in the different C_L after the stall, as shown in Fig. 8. Decrease of C_L due to the stall in the computational result at $\alpha = 15$ deg is larger than that in the experimental results. For this long-cowl nacelle model, the nacelle interference to the flows is relatively large, as discussed in [15]. With the increase of angle of attack, the flow separation on the outboard side of the nacelle becomes larger. The separated and reversed flow interacts with the outboard slat and causes the large separation on the upper surface of the main wing after the nacelle. For this model, the boundary-layer transition on the wing is not a main factor for the stall phenomena.

B. Comparison Between the Experimental and Predicted Transition Locations

The predicted transition locations for TS and CF instabilities and laminar separation bubbles using LSTAB code are discussed. The stability analysis is performed at streamwise sections. Figure 14 shows the spanwise locations at which the transition prediction analyses were conducted.

Figures 15 and 16 show the comparisons of transition lines on the upper surface between experimental and predicted results. The experimental transition lines are identified from the visualized results using china clay. The predicted transition lines are identified using N factor and laminar separation location in the prediction code. For the wind-tunnel tests used in the present study, the threshold of the N factor is expected to be 4.0–6.0, based on the past experimental results. In this study, $N = 4.0$ is used for the threshold. In Figs. 15 and 16, it is assumed that the transition starts just before the location of the laminar separation if the transition due to TS and CF instability does not occur. The transition lines are plotted using the transition locations identified at each section. The compared angles of attack are a little different between the experimental and computational results, due to the wind-tunnel data correction. The small difference does not largely change the transition lines visualized using china clay, and the transitions at $\alpha = 4$ and 5 are nearly identical in the wind-tunnel tests. In the figures, the predicted results using measured C_p in the experiment instead of computed C_p in the CFD computations as the input data for the prediction code are also plotted.

In Fig. 15, transition lines for the inner and outer slats are not plotted, because flows on the upper side are almost laminar until the trailing edge in both experimental and predicted results. Transition lines of experimental results for the main wing are also not plotted, because the flow on the main wing is identified to be turbulent just after the leading edge by china-clay visualization. At this angle of attack, the predicted results using measured C_p and computed C_p are nearly identical, as shown in Fig. 15. In Figs. 15b and 15c, transitions on the main flap and aft flap observed in the experiment are well predicted by the present method. In Fig. 15c, the predicted results on the outer main wing are turbulent just after the leading edge and show good agreement with experimental results. However, there is a difference on the inner main wing in Fig. 15d. In the experimental result, the laminar regions are not observed in visible regions on the inner main wing, whereas transition can occur in the predictions.

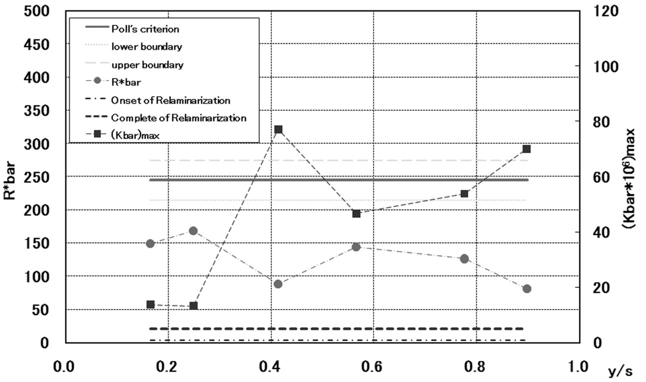

a) Slat

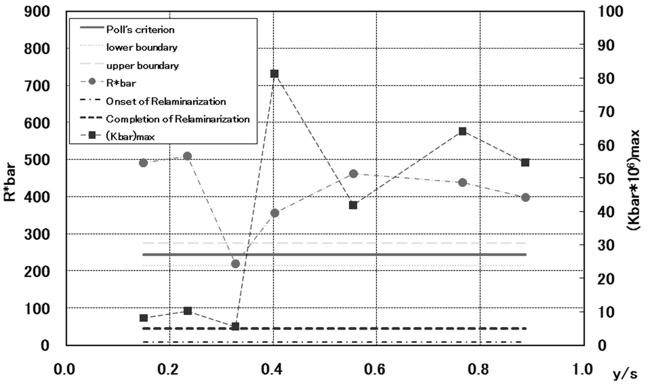

b) Main wing

Fig. 18 Computed $\bar{R}^*$ and $\bar{K}$ for analysis of attachment-line contamination and relaminarization at $\alpha = 10$ deg.

In Fig. 16 at $\alpha = 10$ deg, transition lines for the inner slat are not plotted, because flows on the upper side are almost laminar until the trailing edge in both experimental and predicted results. Transition

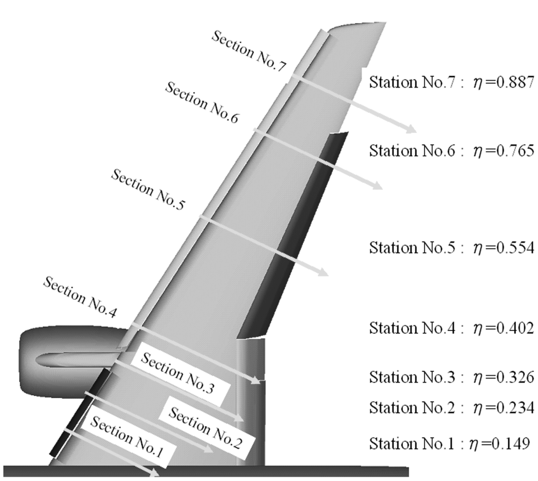

Fig. 17 Analyzed sections for attachment-line contamination and relaminarization.

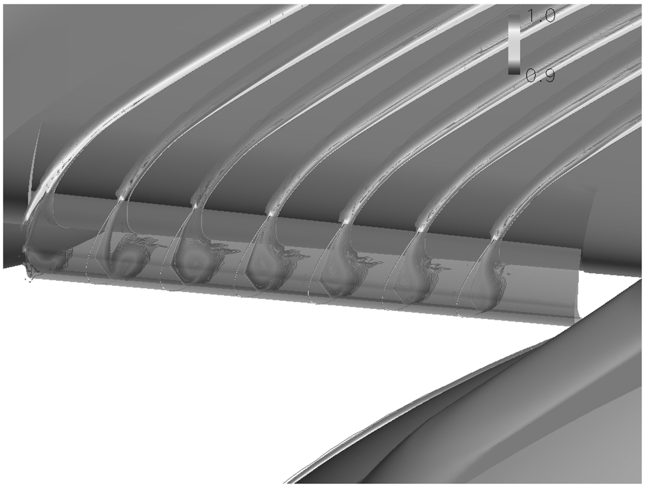

Fig. 19 Total pressure distributions in the inner slat cove at $\alpha = 10$ deg.

Fig. 20 Measured surface flow pattern at $\alpha = 10.55\,\text{deg}$.

lines of experimental results for the inner main wing are also not plotted, because the flow on the inner main wing is identified to be turbulent just after the leading edge. As shown in Fig. 16c, laminar regions appear on the outer slat and outer main wing at $\alpha = 10\,\text{deg}$, whereas they are not observed in the regions at $\alpha = 4\,\text{deg}$ in Fig. 15c. The transitions are well predicted by the present method. In Figs. 16b and 16c, transitions on the main flap are also well predicted, although the predicted results on the inner main flap show slightly earlier transitions. For the aft flap, however, the predicted results using computed C_p show much earlier transitions than the experimental results and predicted results using measured C_p, whereas predicted results using measured C_p show good agreement with experimental results. As shown in Fig. 10a, C_p on the inner flaps shows a large difference with the experimental result. In addition, computed C_p

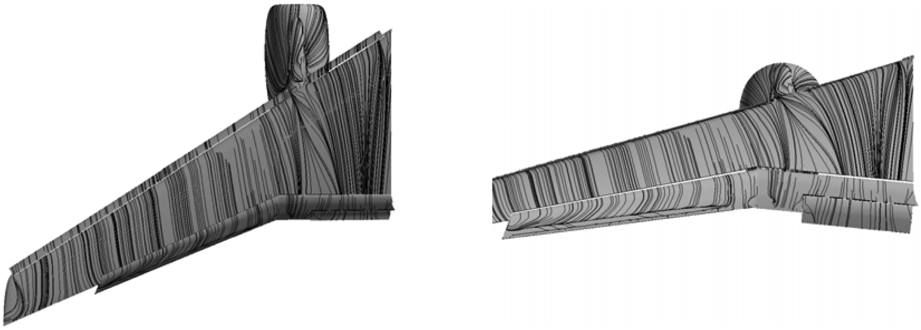

a) Configuration 1: without FTF and without slat support

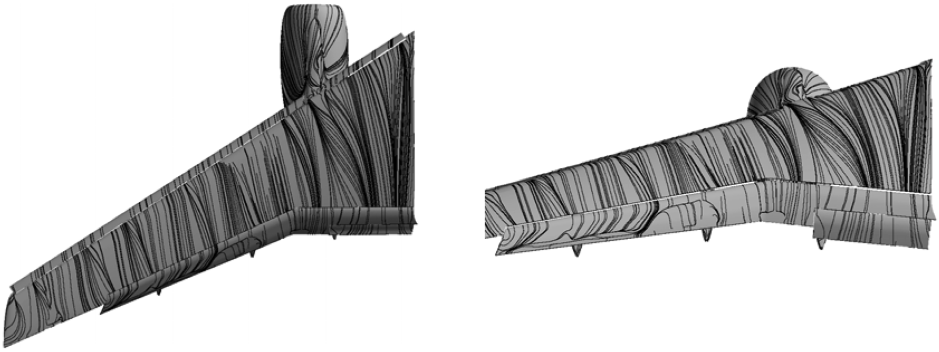

b) Configuration 2: with FTF and without slat support

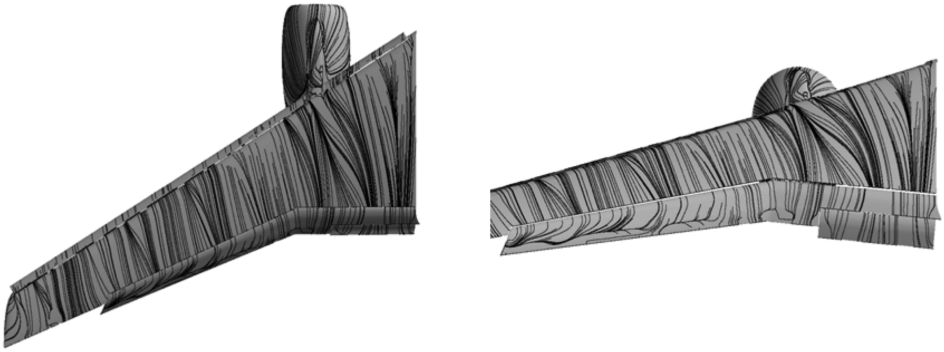

c) Configuration 3: without FTF and with slat support

Fig. 21 Computed surface flow pattern at $\alpha = 10\,\text{deg}$.

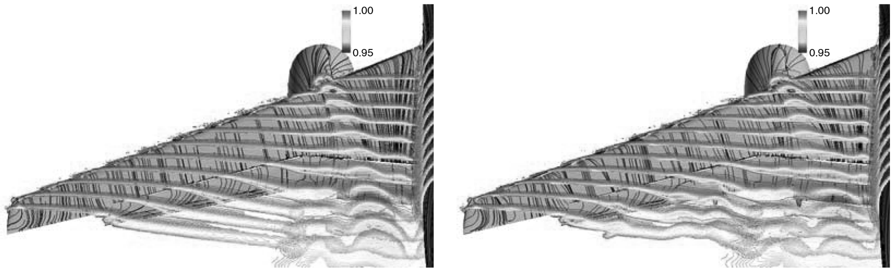

a) Configuration 1: without FTF and without slat support

b) Configuration 2: with FTF and without slat support

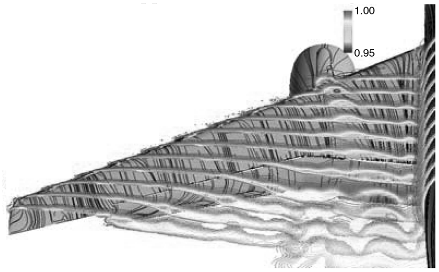

c) Configuration 3: without FTF and with slat support

Fig. 22 Total pressure distributions at $\alpha = 10\,\mathrm{deg}$.

near the leading edge has a little irregularity related to mesh resolution. More consistent C_p has to be obtained in the computations. For the transition prediction on the inner main wing at $\alpha = 10\,\mathrm{deg}$, there is the same inconsistency with the results at $\alpha = 4\,\mathrm{deg}$. In the experimental result, the laminar regions are not observed in visible regions on the inner main wing, whereas laminar regions can be observed in the predictions by computed C_p. The difference of C_p with experimental results at $\alpha = 10\,\mathrm{deg}$ in section BB, shown in Fig. 10a, may cause the different predictions. In addition, the appearance of attachment-line contamination should be also considered, especially on the inner main wing.

Predicted results at $\alpha = 4$ and 10 deg show that most transitions on the upper surface can be caused by laminar separation bubble, not by natural transition. The experimental results of oil flow in Figs. 11 and 12 validate the predicted results. The oil flows show the existence of laminar separation bubble near the expected transition lines.

The predictions of attachment-line contamination and relaminarization are performed at seven sections normal to the leading edges, shown in Fig. 17. Figure 18 shows the computational results of $\bar{R}^*$ and $\bar{K}$ for the slat and main wing at $\alpha = 10\,\mathrm{deg}$. For the slat, the computed values of $\bar{R}^*$ are under the criterion at all span sections. The contamination will not occur on the slat. The values of $\bar{K}$ are over the criterion for relaminarization. However, the relaminarization will not occur physically because of the absence of attachment-line contamination. For the main wing, the values of $\bar{R}^*$ are over the criterion at all spanwise sections, which means that contamination can occur at all spanwise sections. Simultaneously, the values of $\bar{K}$ are over the criterion, and relaminarization can occur at all spanwise sections. These results mean that the laminar regions can exist on the inner main wing if the relaminarization can occur. On the contrary, the laminar regions are not observed on the inner main wing in the experimental result.

The values of $\bar{K}$ for relaminarization parameters computed on the inner main wing are relatively lower than those on the outer main wing and close to the criterion. The acceleration to cause relaminarization is not relatively stronger on the inner main wing, although the values exceed the criterion. In the present prediction, bypass transition due to the wake flow from fore wing elements is not considered. Figure 19 shows the total pressure distributions in the inner slat cove at $\alpha = 10\,\mathrm{deg}$. The three-dimensional vortex in the cove can affect the transition on the leading edge of the main wing. The possibility due to the bypass transition should be evaluated. Further assessments are required with more detail measurements for the transition.

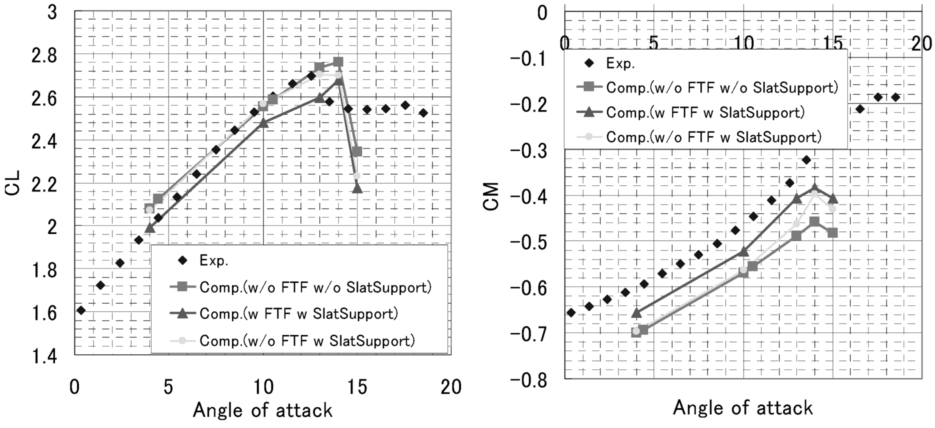

a) C_L–α

b) C_M–α

Fig. 23 Comparison of aerodynamic forces.

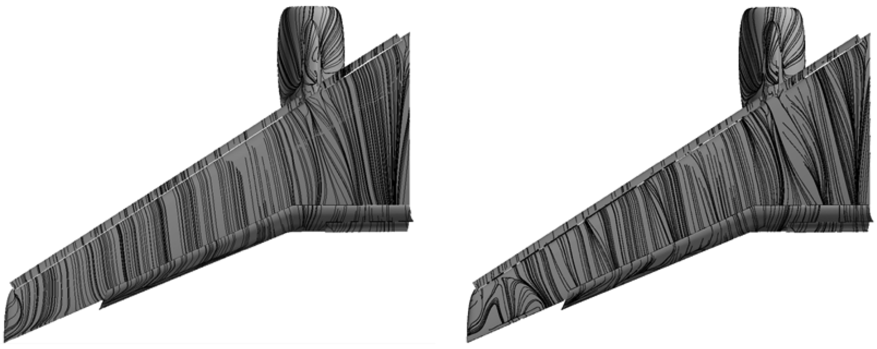

a) Configuration 1: without FTF and without slat support

b) Configuration 3: without FTF and with slat support

Fig. 24 Computed surface flow pattern at $\alpha = 14\,\mathrm{deg}$.

Except for the inner main wing, the present approach with several approximations showed reasonable prediction capability, although the applicability of the e^N method to the laminar flows through relaminarization is not strictly appropriate.

C. Influence of Brackets to Support the High-Lift Devices

The model has eight slat brackets to support the leading-edge slats, one bracket to support the aft flap, and three FTFs, as shown in Fig. 1. To estimate the influence of brackets to support the high-lift devices, computational results on three configurations are compared: without FTFs and slat and aft flap supports (configuration 1 is without FTFs and without slat support), with FTFs and slat and aft flap supports (configuration 2 is with FTFs and with slat support), and without FTFs and with slat and aft flap supports (configuration 3 is without FTFs and with slat support). Fully turbulent flow is assumed in the computations.

Figure 20 shows the experimental surface flow patterns at $\alpha_{\mathrm{corrected}} = 10.55\,\mathrm{deg}$. Figure 21 shows the computed surface flow patterns at $\alpha = 10\,\mathrm{deg}$ on each configuration. The surface flow on the outboard flap for configuration 1 shows the flow separation near the flap trailing edge. In the result of configuration 2 with FTFs and slat supports, the local flow separations also appear on the outboard flap due to the presence of FTFs. Flow separation near the wing tip on the main wing appears in the computation, as seen in the experimental results. The oil-flow patterns by computations with brackets to support high-lift devices show qualitatively good agreement with experimental results, including the local flow separation. In Fig. 21c, the result of configuration 3 with slat supports shows the influences of the wake from slat supports on the main wing. Flow separation near the wing tip on the main wing appears in the computation. This result confirms that the flow separation near the wing tip is caused by the disturbed wake from the slat supports. In addition, the local flow separations on the outboard flap also appear, although FTFs are not installed. Figure 22 shows the total pressure distributions on each configuration. In Fig. 22, a relatively large loss of total pressure appears from the nacelle pylon for all configurations. In the case with slat supports, the disturbed wakes by the slat supports affect the flow separation on the outboard flap, as shown in Fig. 22c.

Figure 23 shows C_L-α and C_M-α. The results of configurations 1 and 3 do not show large changes at moderate angles of attack, whereas the results of configuration 2, which has both FTFs and slat supports, show larger changes for both C_L and C_M. Lift and nose-down pitching moment are reduced on the configuration 2. The results of oil flow in Fig. 21b show larger separation on the outboard flap due to the disturbed flow by FTFs. The reduction of the lift on the outboard flap results in the decrease of lift and nose-down pitching moment.

At higher angles of attack near the stall, the difference between configurations 1 and 3 appears. Figure 24 shows the comparison of oil flows with/without slat supports at $\alpha = 14\,\mathrm{deg}$. The difference clearly appears in the flow separation near the wing tip. This separation due to disturbed wake flow from the outmost slat support near the wing tip caused reduction of C_L at $\alpha = 14\,\mathrm{deg}$ in Fig. 23a and pitch-up $\alpha = 14\,\mathrm{deg}$ in Fig. 23b. Thus, the additional supports have the possibility to largely affect the flow, especially for stall performance. For the validation study, the influences of the additional brackets to support high-lift devices also should be well considered.

V. Conclusions

Three-dimensional flow computations over a realistic high-lift configuration with a flow-through nacelle with a pylon mounted beneath the main wing tested at JAXA were performed to investigate the influences of the boundary-layer transition on the aerodynamic forces, the capability of a transition prediction method, and the influence of brackets to support the high-lift devices.

First, computational results assuming fully turbulent flows and flows with prescribed laminar regions were compared with the wind-tunnel testing data. The amounts of the influence of the boundary-layer transition upon the aerodynamic forces were shown in the computations. The results with laminar regions showed higher C_L, especially at higher angles of attack, and the slope of C_L-α showed better agreement with experimental results, whereas the stall angle of attack and $C_{L\,\max}$ were slightly overestimated in the computations. The consideration of the boundary-layer transition did not improve the stall prediction for the present long-cowl nacelle model. It was shown that the strong nacelle interference can disguise the influence of the boundary-layer transition on the stall phenomena.

Next, the capability of a transition prediction method based on the e^N method and semi-empirical methods was evaluated by comparison with experimental results. In the method, the transitions due to TS and CF instabilities, laminar separation bubbles, attachment-line contamination, and relaminarization were considered for high-lift configurations. Applicability of the method with several approximations, which was combined with RANS CFD, was validated to the complex high-lift flows. Good capability was shown except for on the inner main wing and aft flap. The predicted results using experimental C_p showed better agreement with experimental observations. The results confirmed the capability of the present transition prediction method and showed that more consistent C_p in the computations can improve the transition prediction, especially for aft flap. It was also shown that the possibility of the bypass transition should be investigated on the inner main wing, due to the interferences by the vortices from the slat cove. Further assessments will be required with more detail measurements.

Finally, the influence of brackets to support the high-lift devices on the aerodynamic forces was also discussed. The oil-flow patterns by computations with brackets to support high-lift devices showed qualitatively good agreement with experimental results, including the local flow separation. The disturbed wakes by the slat brackets had a large interference not only on the main wing, but also on the flap. The additional supports have the possibility to largely affect the flow, especially for stall performance. For the validation study, the influences of the additional brackets to support high-lift devices also should be well considered.

References

[1] van Dam, C. P., "The Aerodynamic Design of Multi-Element High-Lift Systems for Transport Airplanes," *Progress in Aerospace Sciences*, Vol. 38, No. 2, 2002, pp. 101–144. doi:10.1016/S0376-0421(02)00002-7

[2] Meredith, P. T., "Viscous Phenomena Affecting High-Lift Systems and Suggestions for Future CFD Development," High-Lift Systems Aerodynamics, AGARD CP 315, Sept. 1993, pp. 19-1–19-8.

[3] Rumsey, C. L., and Ying, S. X., "Prediction of High Lift: Review of Present CFD Capability," *Progress in Aerospace Sciences*, Vol. 38, No. 2, 2002, pp. 145–180. doi:10.1016/S0376-0421(02)00003-9

[4] Johnson, P., Jones, K. M., and Madson, M., "Experimental Investigation of a Simplified 3D High Lift Configuration in Support of CFD Validation," AIAA Paper 2000-4217, Aug. 2000.

[5] Rogers, S. E., Roth, K., and Nash, S. M., "CFD Validation of High-Lift Flows with Significant Wind-Tunnel Effects," AIAA Paper 2000-4218, Aug. 2000.

[6] Hansen, H., Thiede, P., Moens, F., Rudnik, R., and Quest, J., "Overview about the European High Lift Research Programme EUROLIFT," AIAA Paper 2004-0767, Jan. 2004.

[7] Neitzke, K. P., Rudnik, R., and Schröder, A., "Low Speed Validation Tests on Engine/Airframe Integration Within the EC Project EUROLIFT II," AIAA Paper 2005-3704, July 2005.

[8] Rudnik, R., and Germain, E., "Re-No. Scaling Effects on the EUROLIFT High Lift Configurations," AIAA Paper 2007-0752, Jan. 2007.

[9] Krumbein, A., "Automatic Transition Prediction and Application to 3D High-Lift Configurations," AIAA Paper 2006-3164, June 2006.

[10] Perraud, J., and Moens, F., "Transport Aircraft 3D High Lift Wing Numerical Transition Prediction," AIAA Paper 2007-264, Jan. 2007.

[11] Cliquet, J., Houdeville, R., and Arnal, D., "Application of Laminar-Turbulent Transition Criteria in Navier–Stokes Computations," AIAA Paper 2007-515, Jan. 2007.

[12] Toulorge, T., Ponsin, J., Perraud, J., and Moens, F., "Automatic Transition Prediction for RANS Computations Applied to a Generic High-Lift Wing," AIAA Paper 2007-1086, Jan. 2007.

[13] Murayama, M., Yamamoto, K., and Kobayashi, K., "Validation of Computations Around High-Lift Configurations by Structured- and Unstructured- Mesh," *Journal of Aircraft*, Vol. 43, No. 2, Mar.–Apr. 2006, pp. 395–406. doi:10.2514/1.15445

[14] Murayama, M., Imamura, T., Yamamoto, K., and Kobayashi, K., "Comparison of Reynolds-Averaged Navier–Stokes Simulations of Multi-Element High-Lift Configurations," *Journal of Aircraft*, Vol. 44, No. 1, 2007, pp. 175–186. doi:10.2514/1.22838

[15] Murayama, M., Yamamoto, K., Tanaka, K., Yokokawa, Y., and Ito, T., "Numerical Simulation around a High-Lift Configuration of a Civil Aircraft Model," *Proceedings of the Fifth Asian Workshop on Computational Fluid Dynamics* [CD-ROM], Aug. 2006.

[16] Ito, T., Ura, H., Yokokawa, Y., Kato, H., Mitsuo, K., and Yamamoto, K., "High-Lift Device Testing in JAXA 6.5 m × 5.5 m Low-Speed Wind Tunnel," AIAA Paper 2006-3643, June 2006.

[17] Yokokawa, Y., Murayama, M., Ito, T., and Yamamoto, K., "Experimental and CFD of a High-Lift Configuration Civil Transport Aircraft Model," AIAA Paper 2006-3452, June 2006.

[18] Ura, H., Yokokawa, Y., and Ito, T., "Phased Array Measurement of High Lift Devices in Low Speed Wind Tunnel," AIAA Paper 2006-2565, May 2006.

[19] Imamura, T., Enomoto, S., and Yamamoto, K., "3D Unsteady Flow Computations in a Slat Cove Using Large Eddy Simulation," AIAA Paper 2006-2668, May 2006.

[20] Mack, M. D., and McMasters, J. H., "High Reynolds Number Testing in Support of Transport Airplane Development," AIAA Paper 92-3982, 1992.

[21] Langtry, R. B., and Menter, F. R., "Transition Modeling for General CFD Applications in Aeronautics," AIAA Paper 2005-522, 2005.

[22] Chaffin, M. S., and Pirzaheh, S., "Unstructured Navier–Stokes High-Lift Computations on a Trapezoidal Wing," AIAA Paper 2005-5084, June 2005.

[23] Nakahashi, K., Togashi, F., Fujita, T., and Ito, Y., "Numerical Simulations on Separation of Scaled Supersonic Experimental Airplane from Rocket Booster at Supersonic Speed," AIAA Paper 2002-2843, June 2002.

[24] Murayama, M., Togashi, F., Nakahashi, K., Matsushima, K., and Kato, T., "Simulation of Aircraft Response to Control Surface Deflection Using Unstructured Dynamic Grids," *Journal of Aircraft*, Vol. 42, No. 2, Mar.–Apr. 2005, pp. 340–346. doi:10.2514/1.13004

[25] Ito, Y., and Nakahashi, K., "Surface Triangulation for Polygonal Models Based on CAD Data," *International Journal for Numerical Methods in Fluids*, Vol. 39, No. 1, 2002, pp. 75–96. doi:10.1002/fld.281

[26] Sharov, D., and Nakahashi, K., "A Boundary Recovery Algorithm for Delaunay Tetrahedral Meshing," *Proceedings of 5th International Conference on Numerical Grid Generation in Computational Field Simulations*, Mississippi State Univ., Mississippi State, MS, 1996, pp. 229–238.

[27] Ito, Y., and Nakahashi, K., "Improvements in the Reliability and Quality of Unstructured Hybrid Mesh Generation," *International Journal for Numerical Methods in Fluids*, Vol. 45, No. 1, May 2004, pp. 79–108. doi:10.1002/fld.669

[28] Obayashi, S., and Guruswamy, G. P., "Convergence Acceleration of an Aeroelastic Navier–Stokes Solver," *AIAA Journal*, Vol. 33, No. 6, 1995, pp. 1134–1141. doi:10.2514/3.12533

[29] Burg, C., "Higher Order Variable Extrapolation For Unstructured Finite Volume RANS Flow Solvers," AIAA Paper 2005-4999, 2005.

[30] Sharov, D., and Nakahashi, K., "Reordering of Hybrid Unstructured Grids for Lower-Upper Symmetric Gauss-Seidel Computations," *AIAA Journal*, Vol. 36, No. 3, 1998, pp. 484–486. doi:10.2514/2.392

[31] Spalart, P. R., and Allmaras, S. R., "A One-Equation Turbulence Model for Aerodynamic Flows," AIAA Paper 92-0439, Jan. 1992.

[32] Lei, Z., "Effect of RANS Turbulence Models on Computational of Separated Flows over a Wing-Body Configuration," *Transactions of the Japan Society for Aeronautical and Space Sciences*, Vol. 48, Nov. 2005, pp. 150–160.

[33] Matsuo, Y., Nakamura, T., Tsuchiya, M., Ishizuka, T., Fujita, N., Ohkawa, H., Hirabayashi, Y., Takaki, R., Yoshida, M., Nakamura, K., Yamamoto, K., Suematsu, K., and Iwamiya, T., "Numerical Simulator III—Building a Terascale Distributed Parallel Computing Environment for Aerospace Science and Engineering," *Proceedings of the Parallel CFD 2002 Conference*, Elsevier Science, New York, 2003, pp. 187–194.

[34] Yoshida, K., Ogoshi, H., Ishida, Y., and Noguchi, M., "Numerical Study on Transition Prediction Method and Experimental Study on Effect of Supersonic Laminar Flow Control," SP 31, National Aerospace Lab., Tokyo, 1996, pp. 59–79.

[35] Yoshida, K., Ishida, Y., Noguchi, M., Ogoshi, H., and Inagaki, K., "Experimental and Numerical Analysis of Laminar Flow Control at Mach 1.4," AIAA Paper 99-3655, 1999.

[36] Ueda, Y., Ishikawa, H., and Yoshida, K., "Three Dimensional Boundary Layer Transition Analysis in Supersonic Flow Using a Navier–Stokes Code," International Council of the Aeronautical Sciences Paper 2004-2.8.2, 2004.

[37] Iwamiya, T., "A Computational Study on Unmanned Scaled Supersonic Experimental Airplane," AIAA Paper 2002-2841, 2002.

[38] Yoshida, K., Makino, Y., and Shimbo, Y., "An Experimental Study on Unmanned Scaled Supersonic Experimental Airplane," AIAA Paper 2002-2842, 2002.

[39] Kaups, K., and Cebeci, T., "Compressible Laminar Boundary Layers with Suction on Swept and Tapered Wings," *Journal of Aircraft*, Vol. 14, No. 7, July 1977, pp. 661–667. doi:10.2514/3.44614

[40] Poll, D. I. A., "Some Aspects of the Flow Near a Swept Attachment Line with Particular Reference to Boundary Layer Transition," Cranfield Inst. of Technology, Rept. 7805, Cranfield, England, U.K., Aug. 1978.

[41] Beasley, J. A., "Calculation of the Laminar Boundary Layer and Prediction of Transition on a Sheared Wing," Royal Aeronautical Establishment, Rept. 3787, London, Oct. 1973.